Micron 199 (2025) 103908

Contents lists available at ScienceDirect

Micron

journal homepage: www.elsevier.com/locate/micron

Creep damage evaluation of 18Cr–9Ni–3Cu–Nb–N steel by electron backscattered diffraction (EBSD) – comparison of traditional Hough Indexing and novel Spherical Indexing –

Tomotaka Hatakeyama *, Kota Sawada

Research Center for Structural Materials, National Institute for Materials Science, Japan

ARTICLE INFO

Keywords:
Austenitic steel
Creep damage evaluation
EBSD
Spherical Indexing
Misorientation

ABSTRACT

The creep damage evaluation of 18Cr–9Ni–3Cu–Nb–N steel creep interrupted and ruptured at 873 K was performed. Kernel average misorientation (KAM) and grain orientation spread (GOS) values obtained by electron backscattered diffraction (EBSD) through two types of indexing procedures, traditional Hough Indexing (HI) and novel Spherical Indexing (SI), were used as the descriptors of creep damage. The SI resulted in a lower KAM value than that obtained via HI, suggesting improved angular resolution and higher sensitivity for creep damage detection at lower strain levels. The GOS of the virgin sample obtained via SI was also lower than that obtained via HI, whereas that of the crept specimens evaluated via SI and HI were almost identical. Nevertheless, by considering the deviation from the initial value, SI also improved the sensitivity of creep damage detection at the lower strain level using GOS. Therefore, this study revealed the effectiveness of creep damage evaluation with SI compared to that with HI.

1. Introduction

18Cr–9Ni–3Cu–Nb–N steel (KA-SUS304J1HTB, ASME Code Case 2328) is an advanced austenitic stainless steel that has been widely used in boiler tubes for ultra-supercritical plants owing to its excellent creep strength (Semba et al., 2002, 2007). However, recently obtained long-term creep data suggests the creep strength degradation and premature failure in the long-term side (Kimura and Sawada, 2022; Sawada et al., 2021, 2018; Hatakeyama et al., 2021a). Therefore, for the safety management of power plants, creep damage evaluation techniques are used for residual creep life assessment. For example, hardness, strain (measured from the thickness or outside diameter of the tubes), and number density creep voids are used for creep life assessment (Nonaka, 2013; NONAKA and ISOBE, 2009; Rui et al., 2018; SATO et al., 1990; FUJIYAMA, 2009). However, a change in hardness appears at the initial stage of the creep life, whereas that of the others appears only in the latter half of the creep life (FUJIYAMA, 2009). Therefore, a combination of several techniques is required.

Misorientation parameters obtained by electron backscatter diffraction (EBSD) have been suggested as promising descriptors of creep damage (YODA et al., 2017; Kubushiro et al., 2017). Nevertheless, these suggestions have been demonstrated using creep specimens subjected to large creep deformation with a damage ratio greater than 30 %. The reliability of creep damage evaluated via EBSD at a low strain level of less than 5 % is still poor (Rui et al., 2018). In other words, there are few advantages to creep damage evaluation using EBSD than that using hardness, strain, and creep voids in the current situation. For a more reliable life assessment of actual plants, high-precision creep damage evaluation techniques that can detect creep damage of the entire creep life, including lower strain levels, are required.

EBSD can index the crystallographic orientation of the measured points from EBSD patterns (EBSP). Decades of EBSD history, “Hough transformation” has been used to detect the bands, which correspond to the crystallographic plane, in EBSP. However, because of the complex contrast in the bands and the approximation of hyperbolic bands with straight lines, accurate detection of the center of the bands is difficult. This resulted in a misorientation of 0.5–1° in the identified orientation (Shi et al., 2024). Although this angular resolution is sufficient for texture analysis or grain boundary detection, it is fatal for evaluating creep damage, which results in a deviation in the misorientation parameters of less than 1° (YODA et al., 2017).

Recently, “Spherical Indexing” was developed as a novel indexing method (Lenthe et al., 2019; Hielscher et al., 2019). This uses a pattern-matching of a spherical master pattern obtained by dynamical

---

* Correspondence to: 1-2-1, Sengen, Tsukuba, Ibaraki 305-0047, Japan.
E-mail address: hatakeyama.tomotaka@nims.go.jp (T. Hatakeyama).

https://doi.org/10.1016/j.micron.2025.103908
Received 26 May 2025; Received in revised form 21 August 2025; Accepted 21 August 2025

Table 1
Chemical composition of 18Cr–9Ni–3Cu–Nb–N steel (mass%).

	C	Si	Mn	P	S	Ni	Cr	Nb	N	Cu
Requirement	0.07–0.13	≤0.30	≤1.00	≤0.040	≤0.010	7.50–10.50	17.00–19.00	0.30–0.60	0.05–0.12	2.50–3.50
This study	0.08	0.24	0.78	0.030	0.001	8.79	18.68	0.48	0.102	2.92

Table 2
EBSD conditions performed in this study.

Binning	1 × 1	2 × 2	4 × 4	8 × 8	16 × 16
Image size (pixels)	640 × 480	320 × 240	160 × 120	80 × 60	40 × 30
Scan area (µm)	250 × 250				
Step size (µm)	0.5				
Number of points	289289				
File size (GB)	56.3	14.1	3.48	0.85	0.21

simulation and experimentally obtained EBSP to determine the crystallographic orientation. As a result, a significant improvement in the angular resolution to less than 0.1° was expected (Friedrich et al., 2018).

This study was motivated to demonstrate creep life assessment using the misorientation parameters, kernel average misorientation (KAM), and grain orientation spread (GOS), obtained by the Spherical Indexing, and compare the results with traditional Hough transformation-based indexing. Creep-interrupted specimens with relatively low strain levels and a damage ratio of approximately 10 % were subjected to the investigation. Before discussing creep damage, the optimal measurement parameters for Spherical Indexing were investigated using a virgin sample.

2. Experimental procedures

2.1. Material and creep testing

The sample material was 18Cr–9Ni–3Cu–Nb–N steel tube. It was processed by hot extrusion, cold drawing, solution treatment at 1423 K, and water quenching. The chemical composition of the steel reported by steel manufacturer and requirements are listed in Table 1 (T. Friedrich et al., 2016., 2016, 2007).

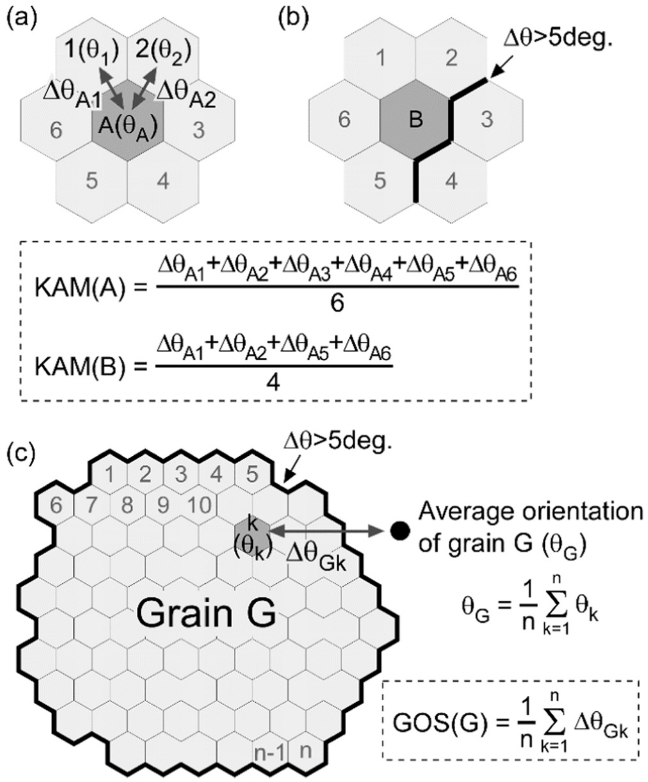

Fig. 2. Schematic illustration of the definition of (a) KAM of a measured point in grain interior, (b) KAM on a measured point vicinity of a grain boundary and (c) GOS.

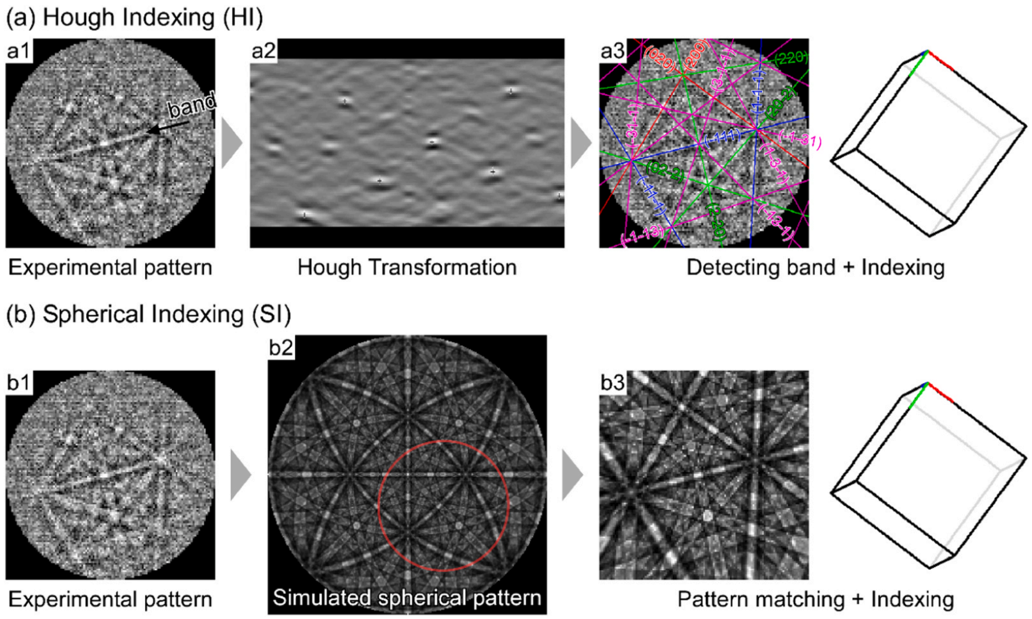

Fig. 1. Indexing procedures of (a) Hough Indexing and (b) Spherical Indexing.

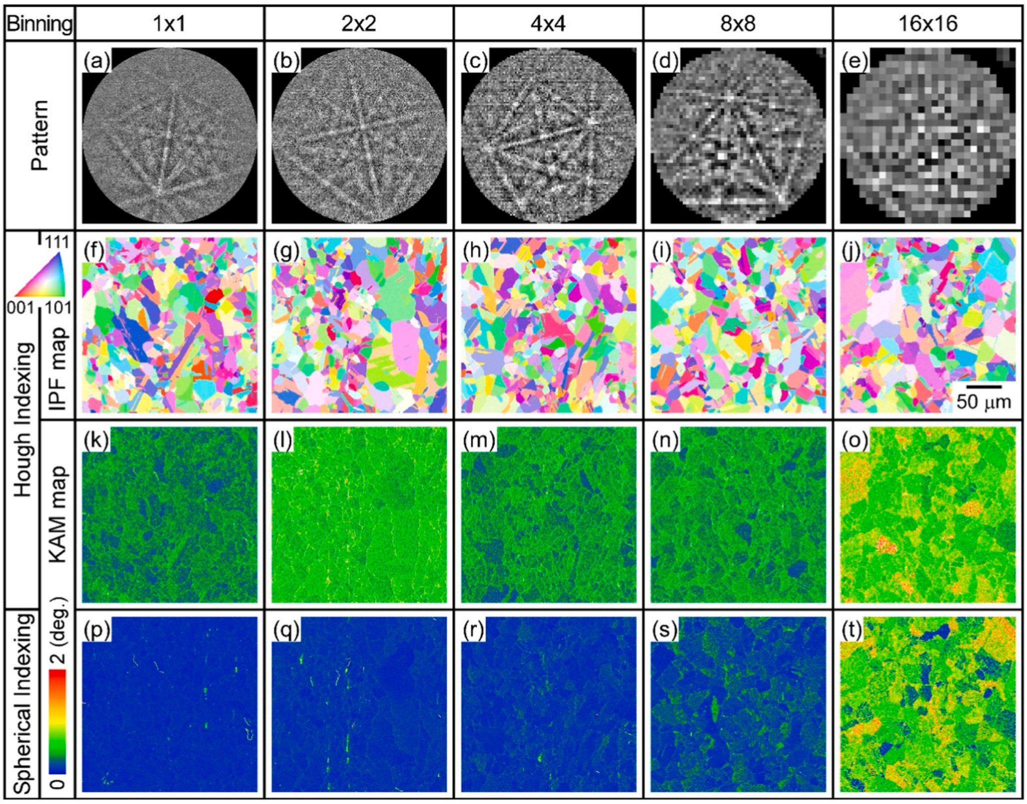

Fig. 3. (a)-(e) Electron backscattered diffraction pattern, (f)-(j) inverse pole figure (IPF) map, (k)-(t) kernel average misorientation (KAM) map obtained from virgin sample through (f)-(o) Hough Indexing and (p)-(t) Spherical Indexing with different binning size of 1 × 1–16 × 16.

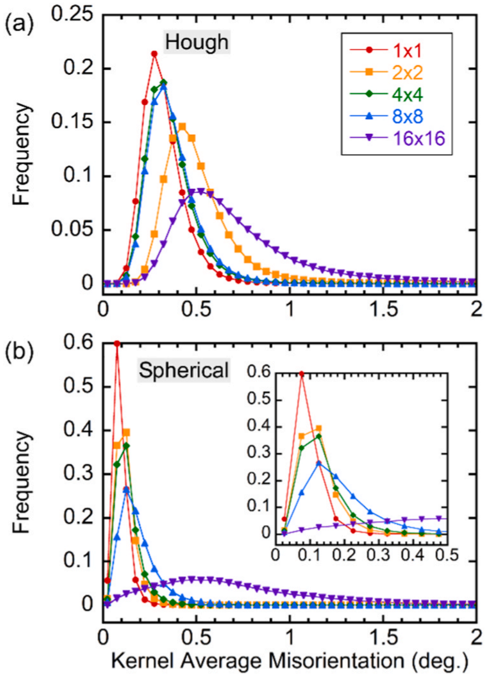

Fig. 4. Histogram of KAM values of virgin sample obtained by (a) Hough Indexing and (b) Spherical Indexing.

Creep specimens with gauge lengths of 30 mm and gauge diameters of 6 mm were machined along the longitudinal direction of the tube. Creep tests were performed at 873 K and 280 MPa until rupture. The time to rupture was 14237.1 h. In addition, five creep interrupted tests were performed at 873 K and 280 MPa for 0, 30, 150, 2000, and 5020 h.

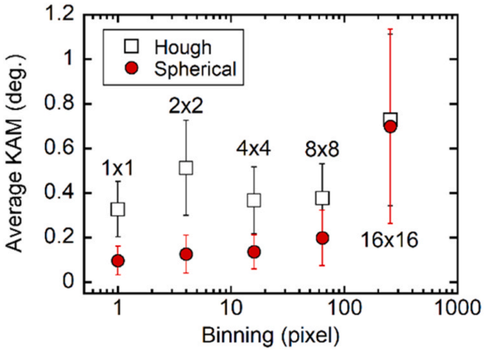

Fig. 5. Effect of binning size on the average KAM values after Hough Indexing and Spherical Indexing.

The test for 0 h indicated that the test was terminated immediately after loading at 280 MPa; only the initial strain was introduced into the specimen. The Vickers hardness of the virgin sample and gauge and grip portions of the crept specimens were measured using a 5 kgf load at five points. The maximum and minimum values were removed, and the average value of the remaining three points was used for evaluation.

2.2. Electron backscatter diffraction (EBSD)

The coupons cut from the virgin sample and gauge portion of the crept specimens were ground using SiC grinding paper, polished with a diamond suspension, and finished using colloidal silica. EBSD (Orion, EDAX) was performed using a scanning electron microscope (SEM, Auriga Laser, Carl Zeiss) with an accelerating voltage of 15 kV and working distance of 20 mm. The EBSP was collected over an area of 250 × 250 μm^2 with a step size of 0.5 µm. The effect of binning was investigated using a virgin sample (Table 2). The EBSD of the gauge

Table 3
Creep testing conditions performed in this study.

Temp. (K)	Stress (MPa)	Time, t (h)	$t/t_{rupture}$ (%)	Elongation, El (%)	$El/El_{rupture}$ (%)	Reduction of area, RA (%)	Note
873	280	0	0	2.36	8.22	3.15	Interrupted
		30	0.21	2.74	9.55	3.58	Interrupted
		150	1.05	2.44	8.50	3.65	Interrupted
		2000	14.05	3.35	11.67	4.41	Interrupted
		5020	35.26	3.98	13.87	6.12	Interrupted
		14237.1	100	28.70	100	40.40	Ruptured

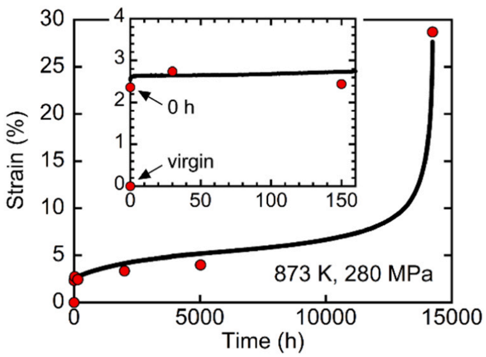

Fig. 6. Creep strain vs time curves of the 18Cr–9Ni–3Cu–Nb–N steel obtained at 873 K under 280 MPa. The time and strain of the virgin sample, interrupted specimens, and ruptured specimen are plotted.

portion of the crept specimens was performed with a fixed binning of 4 × 4. The exposure time was set to 2 ms (500 pps), and the EBSD measurement was completed in approximately 10 min. All EBSP were saved for subsequent analysis using OIM Analysis 9 and OIM Matrix (EDAX).

2.3. Indexing procedures of EBSP

Fig. 1 shows the two types of indexing procedures performed in this study: Hough Indexing (HI) and Spherical Indexing (SI). Indexing requires detection of the band corresponding to the crystallographic plane in the EBSP (Fig. 1(a1) and (b1)). HI uses Hough transformation, which is a mathematical procedure for the transformation of a line to a point (Fig. 1(a2)) (Wright and Adams, 1992). The bright points after Hough transformation correspond to the bands. The orientation of the measured point was determined by comparing the angular relationship of the identified bands with that of the possible crystallographic structure (Fig. 1(a3)). In contrast, SI uses the dynamically simulated spherical pattern of a possible crystal structure (face-centered cubic, a = 0.3650 nm) for indexing (Fig. 1(b2)) (Winkelmann et al., 2007; Callahan and De Graef, 2013). By considering the cross-correlation of the projected experimental pattern with the spherical pattern, the orientation of the measured point can be determined (Fig. 1(b3)) (Lenthe et al., 2019; Hielscher et al., 2019).

2.4. Calculation of misorientation parameter

In this study, the kernel average misorientation (KAM) and grain orientation spread (GOS) were considered as descriptors of creep damage. Both parameters are known to have a linear relationship with the plastic strain provided by dislocation motion (Shen and Efsing, 2018; Nomura et al., 2012). The KAM value is given for each measured point. Because a hexagonal grid was used in this study, each point had six neighboring points. The KAM is defined as the average value of the misorientation between the subject point and neighboring points, as schematically shown in Fig. 2(a). When interfaces with a misorientation greater than 5° (grain boundary) were included, the misorientation value across the interface was removed from the calculation, as schematically shown in Fig. 2(b). In contrast, the GOS value is provided for each grain. Here, a grain is defined as an area surrounded by the interface with a misorientation greater than 5°. The GOS is defined as the average value of the misorientation between the average orientation of the grain and all measured points included in the grain, as schematically shown in Fig. 2(c).

3. Results and discussion

3.1. Effect of pattern resolution on the indexing

When pattern matching is applied for indexing, the EBSP resolution significantly influences the angular resolution. It was revealed that a resolution of 800 × 600 is required to maximize the angular resolution (Friedrich et al., 2018). However, as shown in Table 2, a higher resolution results in an extended file size of tens of GB. Therefore, in this study, the effect of the EBSP resolution (binning size) on the angular resolution was discussed to identify the appropriate EBSP resolution for creep life assessment.

Fig. 3. (a)–(e) and (f)–(j) show the representative EBSP and inverse

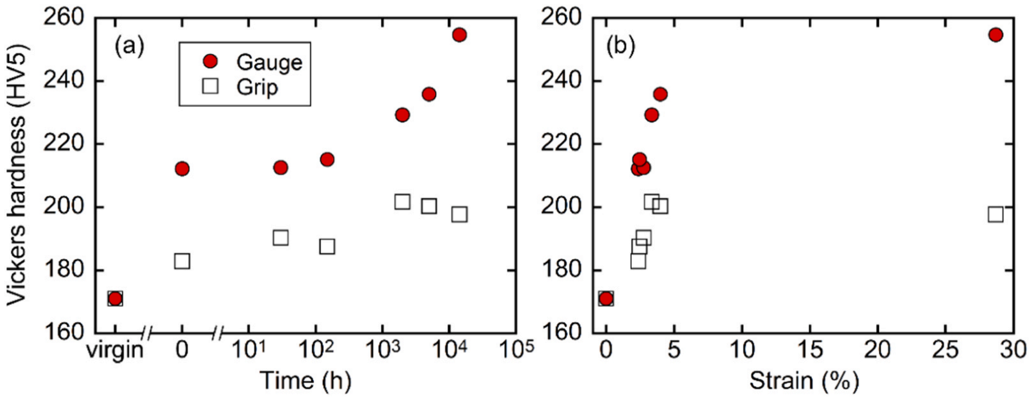

Fig. 7. Change in Vickers hardness of gauge and grip portions as a function of (a) time and (b) strain.

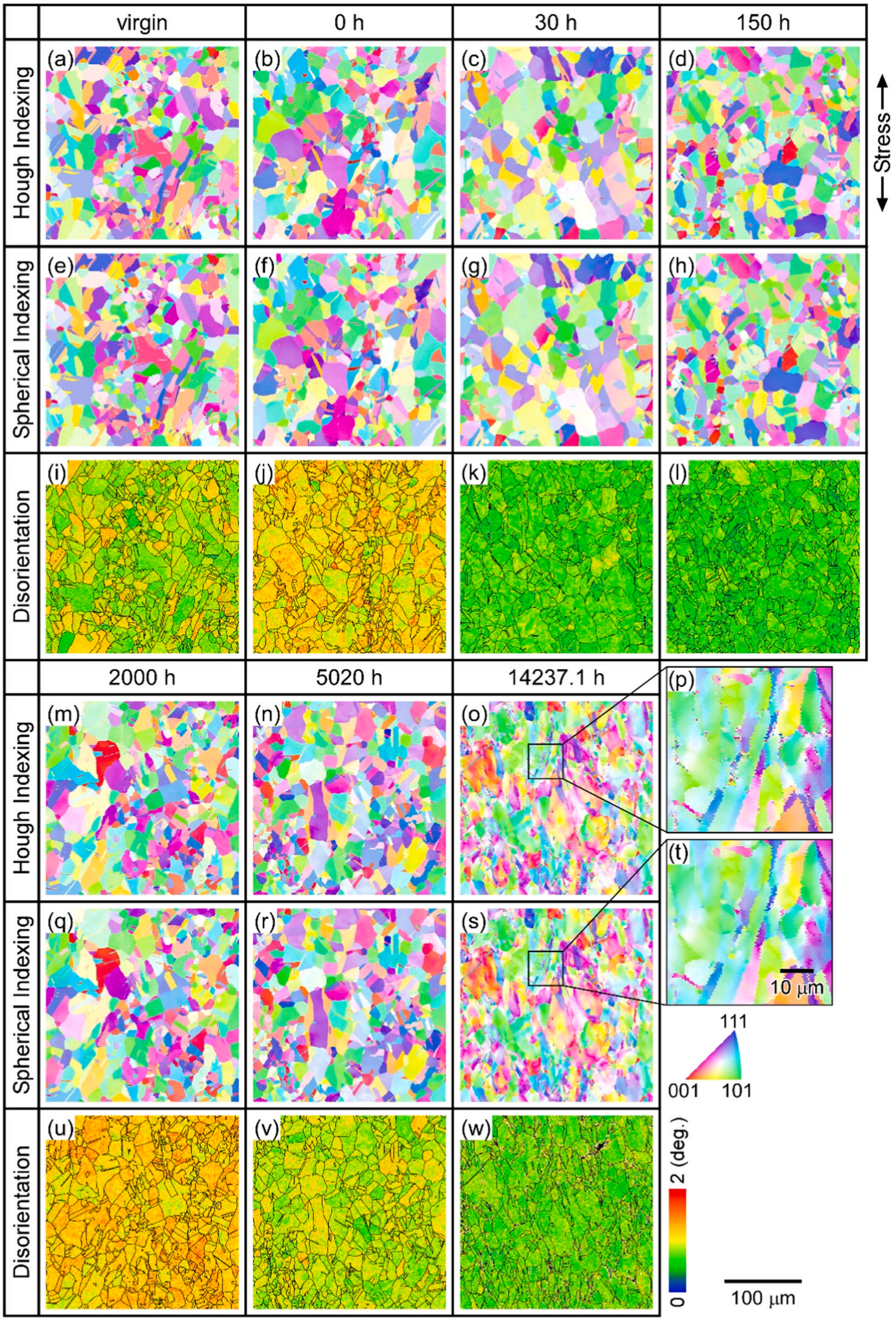

Fig. 8. IPF maps of (a)(e) virgin sample, creep interrupted samples after crept for (b)(f) 0 h, (c)(g) 30 h, (d)(h) 150 h, (m)(q) 2000 h, (n)(r) 5020 h, and (o)(p)(s)(t) creep ruptured sample obtained by (a)–(d), (m)–(p) Hough Indexing and (e)–(h), (q)–(t) Spherical Indexing; point-by-point disorientation between HI and SI of (i) virgin sample, creep interrupted samples after crept for (j) 0 h, (k) 30 h, (l) 150 h, (u) 2000 h, (v) 5020 h, and (w) creep ruptured sample.

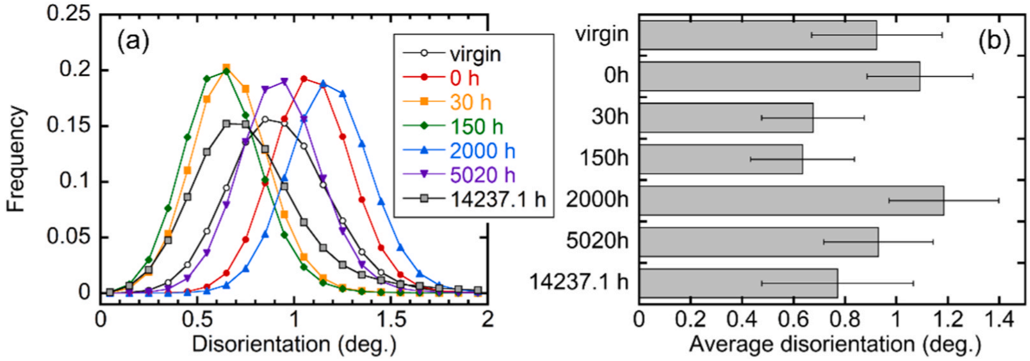

Fig. 9. (a) Histogram of disorientation between HI and SI and (b) average disorientation of each sample.

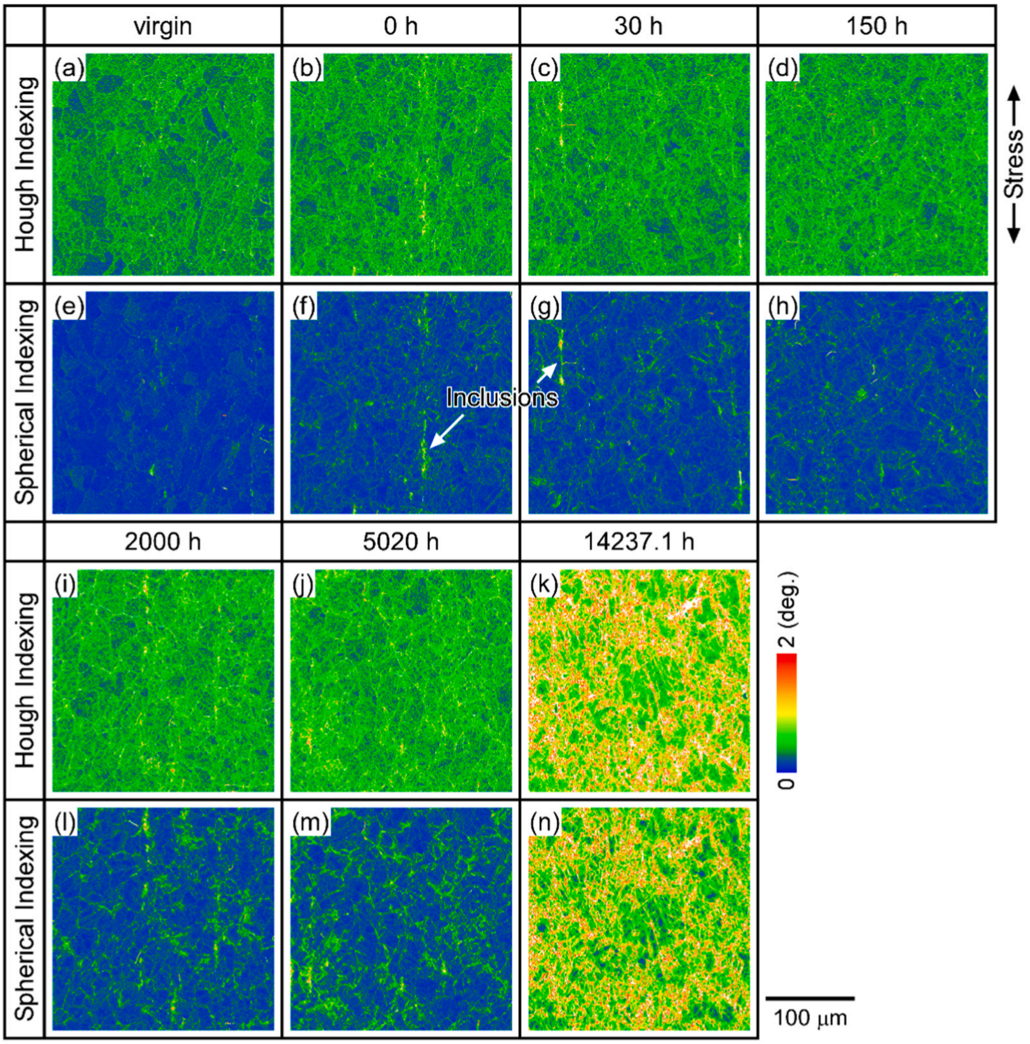

Fig. 10. KAM map of (a)(e) virgin sample, creep interrupted samples after crept for (b)(f) 0 h, (c)(g) 30 h, (d)(h) 150 h, (i)(l) 2000 h, (j)(m) 5020 h, and (k)(n) creep ruptured sample obtained by (a)–(d), (i)–(k) Hough Indexing and (e)–(h), (l)–(n) Spherical Indexing.

pole figure (IPF) maps obtained after the HI of the virgin sample taken with different binning sizes, respectively. Reasonable polycrystalline IPF maps were obtained by the HI for all binning sizes, even in the poor-quality EBSP with a binning of 16 × 16, as shown in Fig. 3(e).

Because the virgin sample was annealed at 1423 K, the strain in the grains should be sufficiently low. Ideally, the KAM value of the virgin sample is close to zero. Fig. 3(k)–(o) and (p)–(t) show the KAM maps of the virgin sample obtained by HI and SI, respectively. As expected, KAM was significantly decreased by SI when binning was 1 × 1–8 × 8, suggesting an improved angular resolution by SI. However, the KAM value with a binning of 16 × 16 was not markedly changed, even by the SI. This suggests that a binning of 16 × 16 (pattern image size: 40 ×30 pixels) should not be used to ensure the angular resolution. The average grain size was determined to be approximately 18 μm based on EBSD measurements.

Fig. 4(a) shows a histogram of the KAM values of the virgin sample

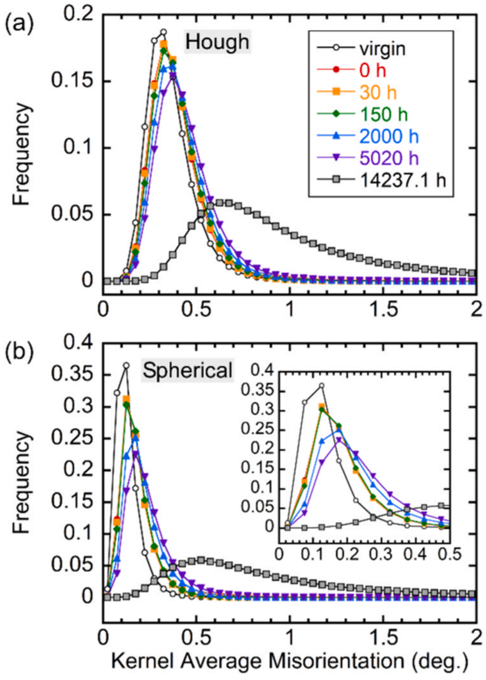

Fig. 11. Histogram of KAM values of the crept samples obtained by (a) Hough Indexing and (b) Spherical Indexing.

obtained by HI. No marked difference in the KAM distribution was observed between the binning of 1 × 1 and 8 × 8 using HI. This indicates that a binning of 1 × 1 is not necessary when considering the intrinsically poor angular resolution of the HI. Nevertheless, binning of 16 × 16 resulted in a higher and broader KAM distribution, suggesting insufficient pattern resolution. Although the reason for the higher KAM value in the binning of 2 × 2 was unclear, calibration trouble for HI was suspected.

Fig. 4(b) shows a histogram of the KAM values of the virgin sample obtained by the SI. The KAM value shifted to a lower angle, and the peak was sharper than that obtained by HI. In addition, as shown in the inset in Fig. 4(b), the peak of KAM shifted to a higher angle with increasing binning size. This indicates the importance of pattern resolution on the angular resolution by the SI. The distribution behavior of the binning of 16 × 16 was not changed by the SI, suggesting an insufficient pattern resolution.

Fig. 5 shows the relationship between the average KAM value and the binning size. Error bars indicate the standard deviation. This also reveals better angular resolution by SI than by HI. Although a smaller binning size improves the angular resolution, a binning of 4 × 4 is considered the appropriate condition in this study by considering the extensive file size (>10 GB/map) of the higher-resolution patterns, as shown in Table 2.

3.2. *Creep damage evaluation by Hough Indexing and Spherical Indexing*

Table 3 shows the creep exposure time (t), elongation (El), and reduction of area (RA) after the creep interruption and rupture tests performed at 873 K under 280 MPa for creep damage evaluation. The damage ratios, $t/t_{rupture}$ and $El/El_{rupture}$, calculated from the time to rupture (14237.1 h) and rupture elongation (28.70 %), respectively, are also tabulated. Fig. 6 shows the creep strain vs time curve obtained from the creep rupture test. The time and strain obtained from the creep-interrupted tests are also plotted. Two plots at 0 h indicate the virgin sample (strain = 0 %) and interrupted after crept for 0 h (strain = 2.36 %). Although the strain after 150 h was smaller than that after 30 h, an overall reproducible creep deformation behavior was confirmed. Creep damage evaluation using EBSD was performed at these seven points. Please note that the microstructure change of the samples during creep has been reported elsewhere (Hatakeyama et al., 2022)

Fig. 7 shows the relationship between the Vickers hardness of the gauge and grip portions of the crept specimens and (a) time and (b) strain. The error bars indicate the standard deviation. Since the grip portion did not undergo deformation, the plot for the grip portion in Fig. 7(b) is not strictly appropriate. However, it was included as a reference for comparison with the corresponding gauge portion. The hardness increased with creep exposure, which was attributed to the increase in dislocation density accompanying creep deformation. As shown in Fig. 7(b), the hardness increased linearly with the strain up to 5020 h. However, the precipitation of the Cu and $M_{23}C_6$ phases during creep has been reported (Hatakeyama et al., 2022). The increase in the hardness of the grip portion during creep indicates that precipitation strengthening also contributes to the hardness. Therefore, it is difficult to separate the consumed creep damage due to deformation from the thermally induced precipitation based on the hardness. In contrast, changes in the misorientation parameters obtained by EBSD are expected to enable an independent evaluation of the consumed creep damage due to deformation.

Fig. 8(a)–(h) and (m)–(t) show the IPF maps of the virgin, creep-interrupted, and ruptured specimens obtained by HI and SI using a binning of 4 × 4. The EBSD of the interrupted specimens was performed around the center of the gauge portion, and that of the ruptured specimen was performed approximately 10 mm from the fracture surface. There were no marked differences between HI and SI. However, some points around the grain boundary where indexing was not successful by HI (Fig. 8(p)) were solved by SI (Fig. 8(t)).

Fig. 8(i)–(l) and (u)–(w) show the point-by-point disorientation

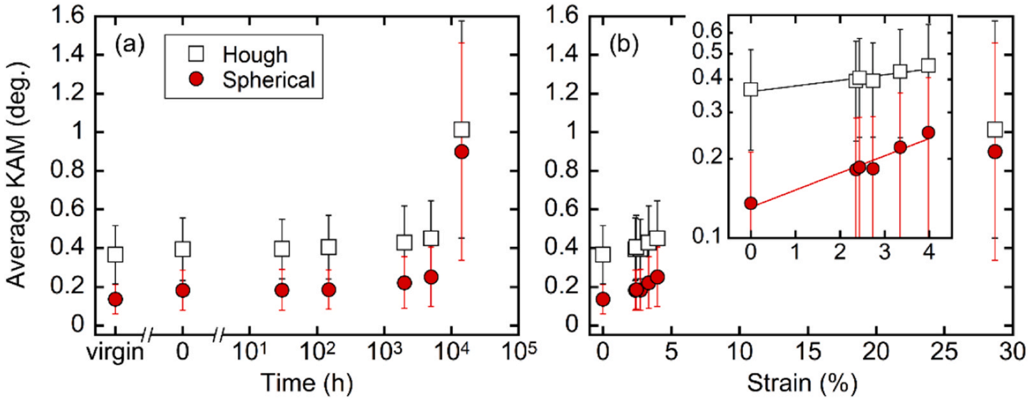

Fig. 12. Change in average KAM value as a function of (a) time and (b) strain.

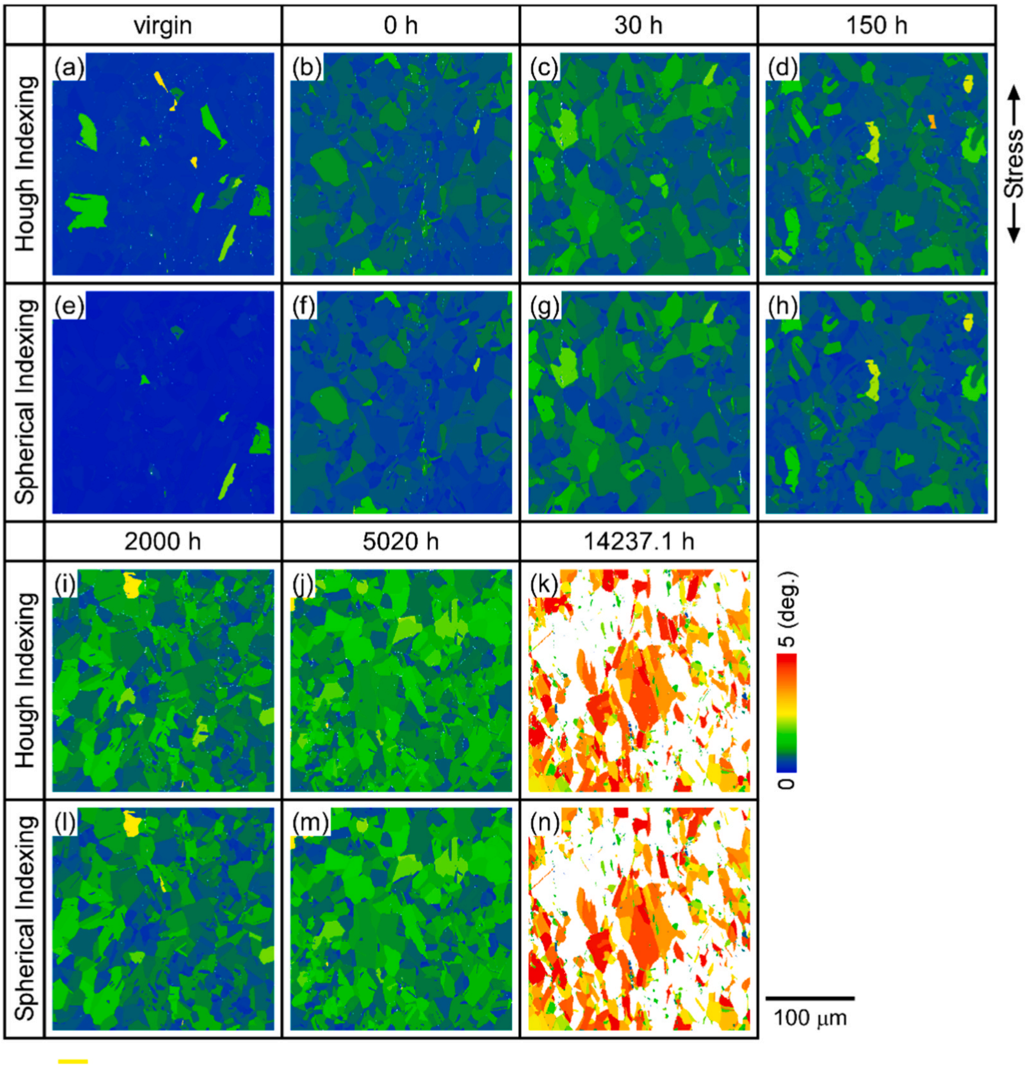

Fig. 13. GOS map of (a)(e) virgin sample, creep interrupted samples after crept for (b)(f) 0 h, (c)(g) 30 h, (d)(h) 150 h, (i)(l) 2000 h, (j)(m) 5020 h, and (k)(n) creep ruptured sample obtained by (a)–(d), (i)–(k) Hough Indexing and (e)–(h), (l)–(n) Spherical Indexing.

between the HI and SI. The black lines indicate high-angle grain boundaries with misorientations greater than 15°. No relationship between the microstructure and disorientation was observed. This implies that disorientation results from the evaluation errors originating from the HI.

Fig. 9(a) and (b) show histograms of the disorientation between the HI and SI and the average disorientation of each sample, respectively. The Error bar in Fig. 9(b) represents the standard deviation of the disorientation. Fig. 9(a) shows that the frequency of the disorientation agrees with the normal distribution. Fig. 9(b) reveals that the average disorientation was 0.6–1.2 ± 0.2°, whereas no relationship between the creep damage and disorientation was observed. In other words, the appearance of disorientation was independent of the sample. Therefore, it was suggested that these disorientation values correspond to the quantitative value of the evaluation error originating from the HI.

Fig. 10 shows the KAM maps of the virgin, creep-interrupted, and ruptured specimens obtained by HI and SI. The high KAM regions in Fig. 10(f) and (g) elongated along the stress direction (longitudinal direction) are inclusions. As confirmed for the virgin sample (Figs. 3–5), KAM was markedly reduced by SI. As a result, the strain distribution in the grain interior was more clearly in the KAM map obtained by SI than that obtained by HI. In addition, the KAM value (obtained via SI) near the grain boundary was higher than that in the grain interior. Although this feature has already been observed using HI (Hatakeyama et al., 2021b), the locally enhanced strain near the grain boundary was clearly visualized as the KAM value via SI.

Fig. 11(a) and (b) show histograms of the KAM values of the virgin sample obtained by HI and SI, respectively. The KAM values obtained by SI were shifted to lower angles, with a sharper peak compared to those obtained by HI. In addition, a peak shift to a higher angle with time was clearly visible in the histogram obtained by SI compared to that obtained by HI. No significant effects of the inclusions observed in Fig. 10(f) and (g) were observed in the histogram.

Fig. 12(a) and (b) show the relationships between the average KAM values and (a) time and (b) strain, respectively. The error bars indicate the standard deviation. These results revealed that the average KAM value obtained by SI was approximately 0.2° lower in the virgin sample than that obtained by HI, and the deviation was reduced with an increase in the creep strain. This indicates that the deviation was due to an evaluation error originating from the HI. In addition, it was suggested that the evaluation error becomes negligible by increasing the strain in the sample when the average value is calculated. The inset in Fig. 12(b) shows the change in KAM with strain at lower strain levels, where the vertical axis is on a logarithmic scale. This revealed that the SI had a steeper slope against strain than the HI. In other words, the SI can sensitively detect minor changes in strain as a deviation from the initial average KAM value compared to the HI.

Fig. 13 shows the GOS maps of the virgin, creep-interrupted, and

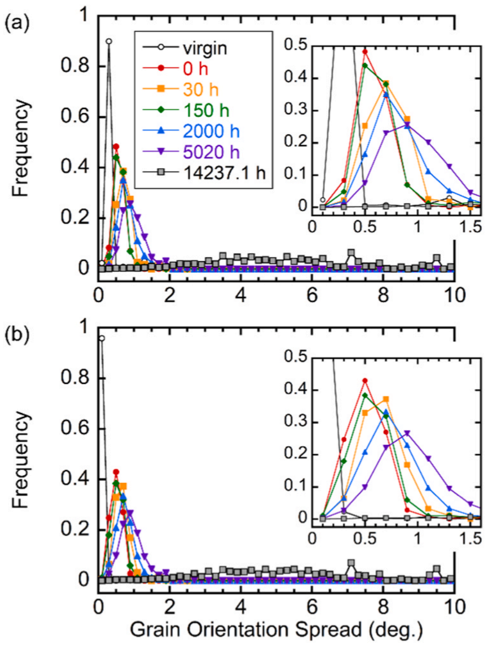

Fig. 14. Histogram of GOS values of the crept samples obtained by (a) Hough Indexing and (b) Spherical Indexing.

ruptured specimens obtained by HI and SI. The GOS of the virgin sample was slightly reduced by SI. However, unlike the KAM map shown in Fig. 10, no marked differences were observed among the crept specimens. Please note that the grains illustrated in white in Fig. 13(k) and (n) have GOS values greater than 5°, which exceeds the maximum value of the scale bar attached adjacent.

Fig. 14(a) and (b) show the histograms of the GOS values of the virgin sample obtained by HI and SI, respectively. The grain size was considered to calculate the frequency. The GOS values obtained by HI and SI were almost identical, except for the virgin sample, which decreased by SI. It was considered that when a certain amount of misorientation exists within a grain, any evaluation error originating from the HI is cancelled during the GOS calculations, as a grain 18 μm in diameter includes more than 1000 measured points. Nevertheless, a clear peak shift to a higher angle with time was visible in the histograms obtained from both HI and SI, as the average GOS value is an excellent descriptor for describing creep damage, even when calculated by HI (YODA et al., 2017).

Fig. 15(a) and (b) show the relationships between the average GOS values and (a) time and (b) strain, respectively. The grain size was weighed to calculate the average GOS value. The error bars indicate the standard deviation. As shown in Figs. 13 and 14, the average GOS value for the virgin sample was reduced by SI. However, those of the crept samples were almost identical due to a sufficiently larger absolute average GOS value compared to evaluation error originating from the HI. The inset in Fig. 15 (b) shows the change in GOS at a lower strain level, where the vertical axis represents a logarithmic scale. This revealed that SI had a steeper slope against strain than HI. In other words, similar to the average KAM value, the SI can sensitively detect minor changes in strain, as a deviation from the initial average GOS value compared to the HI, due to its lower initial value.

In conclusion, the advantages of KAM and GOS are summarized. In evaluating crept specimens, KAM exhibited significant differences between HI and SI. This indicates that a KAM map effectively evaluates the relationship between the microstructure and locally accumulated strain, leveraging SI's high angular resolution. Conversely, GOS is considered more suitable for creep life assessment, especially at low-strain levels due to its larger absolute values and greater deviations against strain.

4. Conclusions

4.1. Effect of pattern resolution on the indexing

- The use of a smaller binning size (higher pattern resolution) yields better angular resolution via Spherical Indexing but results in a larger file size.
- A binning of 4 × 4 (160 ×120 pixels) was considered an appropriate pattern resolution to withstand the angular resolution and acceptable file size.

4.2. Creep damage evaluation by Hough Indexing and Spherical Indexing

- Spherical Indexing can minimize evaluation errors in the indexing process, resulting in enhanced angular resolution and improved reliability of misorientation parameters, such as kernel average misorientation (KAM) and grain orientation spread (GOS), especially at low strain levels with an average misorientation value of less than 1°.
- The average KAM and average GOS values obtained by Spherical Indexing were suggested to be beneficial descriptors for sensitively detecting minor creep strains of less than 5 %.

CRediT authorship contribution statement

Tomotaka Hatakeyama: Writing – original draft, Visualization, Resources, Investigation, Funding acquisition, Data curation, Conceptualization. **Kota Sawada:** Writing – review & editing, Supervision, Project administration.

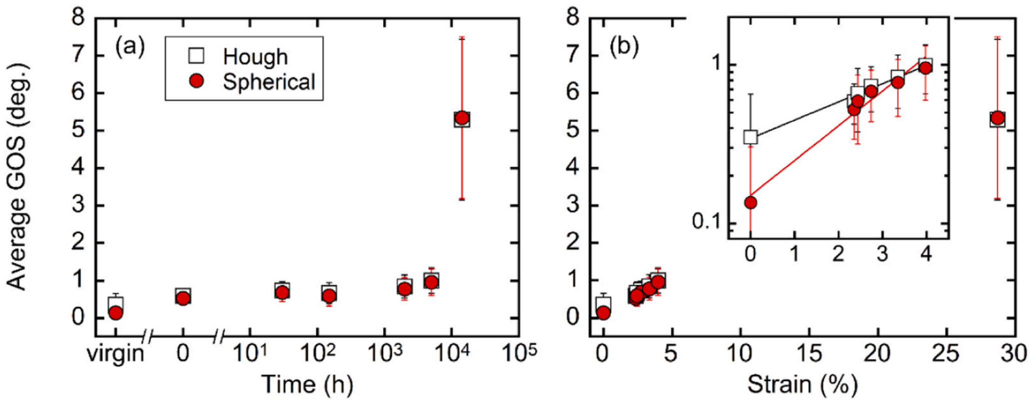

Fig. 15. Change in average GOS value as a function of (a) time and (b) strain.

Declaration of Competing interest

The authors declare that they have no known competing financial interests or personal relationships that could have appeared to influence the work reported in this paper.

Acknowledgement

The authors thank Mr. Yasushi Taniuchi, Dr. Kaoru Sekido, and Mr. Takehiro Nojima for their support with creep testing; and Dr. Toru Hara, Mr. Taku Moronaga, Ms. Yuka Hara, and Ms. Akiko Nakamura for their support with microstructural observations (all at NIMS). This work was supported by JSPS KAKENHI [grant number JP22K14504].

Data availability

Data will be made available on request.

References

Callahan, P.G., De Graef, M., 2013. Dynamical electron backscatter diffraction patterns. Part I: pattern simulations. Microsc. Microanal. 19, 1255–1265. https://doi.org/10.1017/S1431927613001840.

Friedrich, T., Bochmann, A., Dinger, J., Teichert, S., 2018. Application of the pattern matching approach for EBSD calibration and orientation mapping, utilising dynamical EBSP simulations. Ultramicroscopy 184, 44–51. https://doi.org/10.1016/j.ultramic.2017.10.006.

FUJIYAMA, K., 2009. I: overview. J. Soc. Mater. Sci. Jpn. 58, 443–448. https://doi.org/10.2472/jsms.58.443.

Hatakeyama, T., Sawada, K., Hara, T., Sekido, K., Kimura, K., 2021a. Three-dimensional analysis of the precipitation behavior of 18Cr–9Ni–3Cu–Nb–N steel at 973 k. Scr. Mater. 200, 113904. https://doi.org/10.1016/j.scriptamat.2021.113904.

Hatakeyama, T., Sawada, K., Sekido, K., Hara, T., Kimura, K., 2021b. Influence of dynamic microstructural changes on the complex creep deformation behavior of 25Cr–20Ni–Nb–N steel at 873 k. Mater. Sci. Eng. A 814, 141270. https://doi.org/10.1016/j.msea.2021.141270.

Hatakeyama, T., Sawada, K., Sekido, K., Hara, T., Kimura, K., 2022. Microstructural factors of the complex creep rate change in 18Cr–9Ni–3Cu–Nb–N steel. Mater. Sci. Eng. A 831. https://doi.org/10.1016/j.msea.2021.142225.

Hielscher, R., Bartel, F., Britton, T.B., 2019. Gazing at crystal balls: electron backscatter diffraction pattern analysis and cross correlation on the sphere. Ultramicroscopy 207, 112836. https://doi.org/10.1016/j.ultramic.2019.112836.

2007 KA-SUS304J1HTB, The material specification in the Technical Regulation of Equipment for Thermal Power Plant, 2007.

Kimura, K., Sawada, K., 2022. Creep deformation property and creep life evaluation of Super304H. J. Press Vessel Technol. 144, 1–2. https://doi.org/10.1115/1.4052397.

Kubushiro, K., Shioda, Y., Nomura, K., 2017. Creep degradation for austenitic stainless steel in KA-SUS304J1HTB. J. Soc. Mater. Sci. 66, 179–184.

Lenthe, W.C., Singh, S., Graef, M.De, 2019. A spherical harmonic transform approach to the indexing of electron back-scattered diffraction patterns. Ultramicroscopy 207, 112841. https://doi.org/10.1016/j.ultramic.2019.112841.

2016 NIMS Creep Data Sheet, Metallographic Atlas of Long-Term Crept Materials, No. M-11, 2016.

Nomura, K., Kubushiro, K., Sakakibara, Y., Takahashi, S., Yoshizawa, H., 2012. Effect of grain size on plastic strain analysis by EBSD for austenitic stainless steels with tensile strain at 650°C. J. Soc. Mater. Sci. Jpn. 61, 371–376. https://doi.org/10.2472/jsms.61.371.

Nonaka, I., 2013. The frontier of technology development in remaining life assessment for high temperature components. J. Soc. Mater. Sci. Jpn. 62, 50–56. https://doi.org/10.2472/jsms.62.50.

Nonaka, I., Isobe, N., 2009. Degradation/ damage measurement and life assessment of High-Temperature components. J. Soc. Mater. Sci. Jpn. 58, 533–539. https://doi.org/10.2472/jsms.58.533.

Rui, S.S., Shang, Y.B., Fan, Y.N., Han, Q.N., Niu, L.S., Shi, H.J., Hashimoto, K., Komai, N., 2018. EBSD analysis of creep deformation induced grain lattice distortion: a new method for creep damage evaluation of austenitic stainless steels. Mater. Sci. Eng. A 733, 329–337. https://doi.org/10.1016/j.msea.2018.07.058.

SATO, T., KOYAMA, T., NOMURA, M., SUGAI, S., 1990. Creep damage evaluation of boiler tubes. J. Soc. Mater. Sci. Jpn. 39, 483–488. https://doi.org/10.2472/jsms.39.483.

Sawada, K., Sekido, K., Murata, M., Kamihira, K., Kimura, K., 2018. Precipitation behavior during aging and creep in 18Cr–9Ni–3Cu–Nb–N steel. Mater. Charact. 141, 279–285. https://doi.org/10.1016/j.matchar.2018.04.055.

Sawada, K., Hatakeyama, T., Sekido, K., Kimura, K., 2021. Microstructural changes and creep-strength degradation in 18Cr-9Ni-3Cu-Nb-N steel. Mater. Charact. 178, 111286. https://doi.org/10.1016/j.matchar.2021.111286.

Semba, H., Sawaragi, Y., Ogawa, K., Natori, A., Kan, T., 2002. Development of “SUPER304H” austenitic stainless steel tubes with high temperature strength for USC boilers. Mater. Jpn. 41, 120–122. https://doi.org/10.2320/materia.41.120.

Semba, H., Okada, H., Ogawa, K., Iseda, A., Yamadera, Y., 2007. Development of SUPER304H (KA-SUS304J1HTB) austenitic stainless tubes with high elevated temperature strength for USC boilers. Mater. Jpn. 46, 99–101. https://doi.org/10.2320/materia.46.99.

Shen, R.R., Efsing, P., 2018. Overcoming the drawbacks of plastic strain estimation based on KAM. Ultramicroscopy 184, 156–163. https://doi.org/10.1016/j.ultramic.2017.08.013.

Shi, Q., Loisnard, D., Li, Y., Chen, Z., Wang, H., Roux, S., 2024. Accuracy assessment of crystal orientation indexations by EBSD. Meas. Sci. Technol. 35, 045030. https://doi.org/10.1088/1361-6501/ad204d.

Winkelmann, A., Trager-Cowan, C., Sweeney, F., Day, A.P., Parbrook, P., 2007. Many-beam dynamical simulation of electron backscatter diffraction patterns. Ultramicroscopy 107, 414–421. https://doi.org/10.1016/j.ultramic.2006.10.006.

Wright, S.I., Adams, B.L., 1992. Automatic analysis of electron backscatter diffraction patterns. Metall. Trans. A 23, 759–767. https://doi.org/10.1007/BF02675553.

YODA, R., KAMAYA, M., KIMURA, H., OHTANI, T., FUJIYAMA, K., 2017. Round robin test using EBSD for creep damage evaluation. J. Soc. Mater. Sci. Jpn. 66, 130–137. https://doi.org/10.2472/jsms.66.130.